

## RESEARCH ARTICLE

## BATTERIES

# Black phosphorus composites with engineered interfaces for high-rate high-capacity lithium storage

Hongchang Jin<sup>1\*</sup>, Sen Xin<sup>2,3\*</sup>, Chenghao Chuang<sup>4</sup>, Wangda Li<sup>3</sup>, Haiyun Wang<sup>1</sup>, Jian Zhu<sup>5</sup>, Huanyu Xie<sup>1</sup>, Taiming Zhang<sup>1</sup>, Yangyang Wan<sup>1</sup>, Zhikai Qi<sup>1</sup>, Wensheng Yan<sup>6</sup>, Ying-Rui Lu<sup>7</sup>, Ting-Shan Chan<sup>7</sup>, Xiaojun Wu<sup>1</sup>, John B. Goodenough<sup>3</sup>, Hengxing Ji<sup>†</sup>, Xiangfeng Duan<sup>8†</sup>

High-rate lithium (Li) ion batteries that can be charged in minutes and store enough energy for a 350-mile driving range are highly desired for all-electric vehicles. A high charging rate usually leads to sacrifices in capacity and cycling stability. We report use of black phosphorus (BP) as the active anode for high-rate, high-capacity Li storage. The formation of covalent bonds with graphitic carbon restrains edge reconstruction in layered BP particles to ensure open edges for fast Li<sup>+</sup> entry; the coating of the covalently bonded BP-graphite particles with electrolyte-swollen polyaniline yields a stable solid-electrolyte interphase and inhibits the continuous growth of poorly conducting Li fluorides and carbonates to ensure efficient Li<sup>+</sup> transport. The resultant composite anode demonstrates an excellent combination of capacity, rate, and cycling endurance.

Lithium ion batteries (LIBs) are increasingly important for diverse applications, including electrical vehicles. However, today's batteries can only provide a limited power density (e.g., ~100 to 300 W kg<sup>-1</sup> at the cell level) and typically require a relatively long charging time (hours or longer) for safe operation (1, 2). To improve charging rate, specific energy, and battery lifetime, anode materials with a high Li storage capacity, high rate capability, and high electrochemical stability are essential. Binary composites consisting of a Li<sup>+</sup> insertion host (e.g., graphite) for fast and stable Li storage and an alloying element (e.g., silicon) for high lithiation capacity have been developed (3) with a reversible capacity of 517 mA-hour g<sup>-1</sup> (with respect to the composite mass) and an areal capacity of >3.3 mA-hour cm<sup>-2</sup>, showing commercial viability for next-generation LIBs (4). However, such a capacity is only achieved at a relatively

low current density of 0.26 A g<sup>-1</sup> with a full charging time of ~2 hours. To be competitive with 5-min refuel time for conventional combustion engine vehicles, all-electric road vehicles require LIB cells that reach a full charge

of 350 W-hour kg<sup>-1</sup> after a comparable duration. Achieving these goals requires anode materials that can be charged to a specific capacity of 350 to 400 mA-hour g<sup>-1</sup> at a charge-discharge current density of >5 A g<sup>-1</sup> (5). To this end, it is essential to develop an electrode material simultaneously featuring high theoretical capacity along with the excellent electron conductivity and Li<sup>+</sup> diffusivity that are necessary for rapid charge (6).

Layered black phosphorus (BP) exhibits several attractive features for high-rate, high-capacity Li storage. Through a three-electron alloying reaction with Li<sup>+</sup>, BP can theoretically deliver a gravimetric capacity of 2596 mA-hour g<sup>-1</sup> (7, 8), which is only bettered by Si (4200 mA-hour g<sup>-1</sup>) and Li metal (3860 mA-hour g<sup>-1</sup>) (9). The large capacity of BP helps offset its relatively high voltage loss versus (Li/Li<sup>+</sup>) (~0.7 V on average) to render a high specific energy density according to the equation  $E = V(q) \times Q(I_{\text{dis}})$ , where  $V(q)$  is the mean cell voltage versus state of charge  $q$  and  $Q(I_{\text{dis}})$  is the capacity density for a given discharge current, with  $I_{\text{dis}}$  calculated as  $dq/dt$ . Additionally, the electrical conductivity of BP is ~300 S m<sup>-1</sup> (10), four orders of magnitude greater than that of silicon ( $6.7 \times 10^{-2}$  S m<sup>-1</sup>) (11); the Li<sup>+</sup> diffusion barrier along the zigzag direction of layered BP is only 0.08 eV (12),

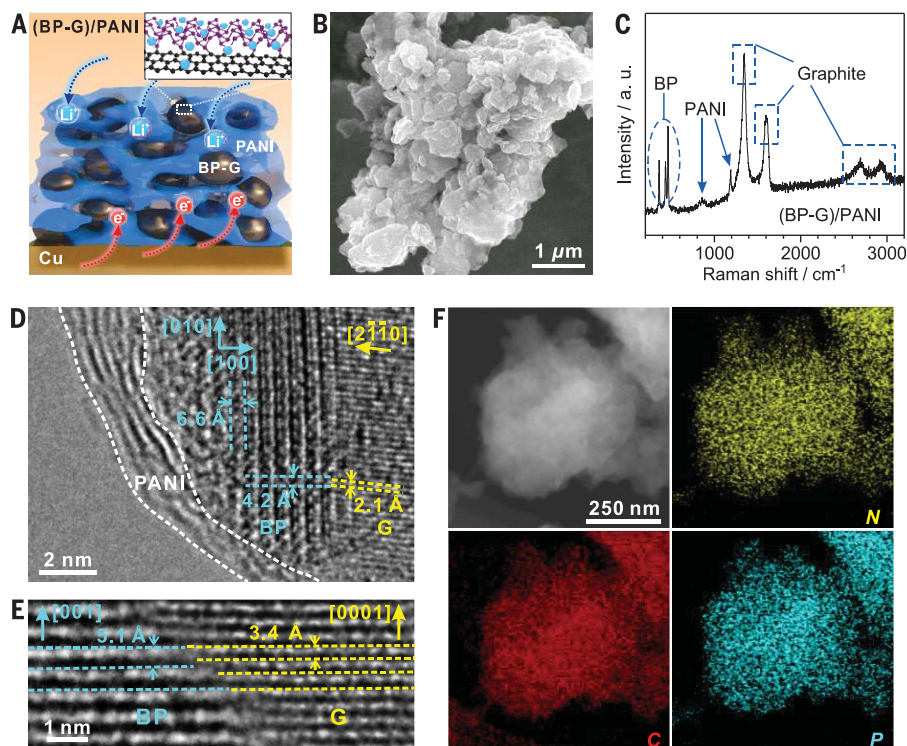


**Fig. 1. Structure of (BP-G)/PANI.** (A) Schematic of (BP-G)/PANI. (B and C) SEM image (B) and Raman spectrum (C) of (BP-G)/PANI. a.u., arbitrary units. (D) TEM image showing the crystalline domains of BP and a graphite flake covered with PANI. (E) High-resolution TEM image showing the merge of basal planes of BP and graphite. Every two BP layers match with three graphene layers. (F) Dark-field TEM image and P, C, and N elemental maps of (BP-G)/PANI.

<sup>1</sup>Hefei National Laboratory for Physical Sciences at the Microscale, CAS Key Laboratory of Materials for Energy Conversion, School of Chemistry and Materials Science, University of Science and Technology of China, Hefei 230026, China. <sup>2</sup>CAS Key Laboratory of Molecular Nanostructure and Nanotechnology, Beijing National Laboratory for Molecular Sciences (BNLMS), Institute of Chemistry, Chinese Academy of Sciences (CAS), Beijing 100190, China. <sup>3</sup>Department of Mechanical Engineering, The University of Texas at Austin, Austin, TX 78712, USA. <sup>4</sup>Department of Physics, Tamkang University, Tamsui 251, New Taipei City, Taiwan. <sup>5</sup>State Key Laboratory for Chemo/Biosensing and Chemometrics, College of Chemistry and Chemical Engineering, Hunan University, Changsha 410082, China. <sup>6</sup>National Synchrotron Radiation Laboratory, University of Science and Technology of China, Hefei 230029, China. <sup>7</sup>National Synchrotron Radiation Research Center, 300 Hsinchu, Taiwan. <sup>8</sup>Department of Chemistry and Biochemistry, University of California, Los Angeles, CA 90095, USA.

\*These authors contributed equally to this work.

†Corresponding author. Email: jihengx@ustc.edu.cn (H.J.); xduan@chem.ucla.edu (X.D.)

considerably lower than that in silicon (0.58 eV) (13). These combined features have invited investigations of the rate of  $\text{Li}^+$  diffusion in BP. Studies to date show a faster  $\text{Li}^+$  diffusion in bulk BP than in silicon or other conventional anode materials. However, an edge atom reconstruction near the zigzag diffusion channel of BP nanoflakes hinders the kinetics of  $\text{Li}^+$  transfer across the surface (14). Additionally, the volume change of BP during charge–discharge cycles renders the solid–electrolyte interphase (SEI) unstable, leading to poor cycling performance (7).

We present a BP-graphite (BP-G) hybrid with a covalently bonded BP-G interface, to prevent edge reconstruction and ensure efficient  $\text{Li}^+$  insertion and diffusion, and a thin polyaniline (PANI) polymer gel coating swollen by electrolytes to prevent the continued formation and buildup of less-conductive Li fluorides and carbonates, leading to a stable SEI that is more conductive for  $\text{Li}^+$ . The designed (BP-G)/PANI

composite with optimized interface for  $\text{Li}^+$  conduction delivers a combination of high rate and high capacity with robust cycling stability.

### Structural characterization of (BP-G)/PANI composite

The (BP-G)/PANI composites (Fig. 1A) were fabricated by ball milling a mixture of BP and graphite and then in situ polymerization of PANI (materials and methods, figs. S1 and S2, and table S1). The scanning electron microscopy (SEM) image of the composite shows aggregates of (BP-G)/PANI particles (Fig. 1B). The Raman spectrum shows intense bands of the  $\text{A}_g^1$ ,  $\text{B}_{2g}$ , and  $\text{A}_g^2$  vibration modes of BP at 363, 440, and 467  $\text{cm}^{-1}$ , respectively (Fig. 1C) (15). The Raman bands centered at 850 and 1200  $\text{cm}^{-1}$  are attributed to PANI (16), and those at 1330 and 1590  $\text{cm}^{-1}$  are the D and G bands of graphite, respectively (17).

The transmission electron microscopy (TEM) image (Fig. 1D) obtained at the edge of a (BP-G)/

PANI particle presents three domains with different crystalline features. The crystal domain in the particle center shows lattice fringes with d-spacings of 6.6 and 4.2 Å, corresponding to the (100) and (010) lattice planes of BP crystal, respectively (8). The crystal domain on the right-hand side shows fringes with a d-spacing of 2.1 Å, corresponding to the (10 $\bar{1}$ 0) plane of graphite (18). PANI is amorphous and covers the surface of the BP-G domain (Fig. 1D).

The lattice-resolved TEM image also reveals that the d-spacings across the basal planes of BP and graphite are 5.1 and 3.4 Å, respectively, with every two BP layers matching with three graphene layers (Fig. 1E). Dislocations are evident at the interface due to mismatched layer numbers. Nonetheless, with weak van der Waals interaction across the basal planes, the strain caused by the dislocations may be released near the grain boundary, and the crystal structures away from the grain boundary largely retain nearly ideal structures (19). These results indicate

**Fig. 2. Electrochemical performance of (BP-G)/PANI.** (A and B) Galvanostatic discharge and charge profiles of different cycles (A) and measured at different current densities (B). (C) Cycling performance of (BP-G)/PANI measured at current densities of 2.6, 5.2, and 13  $\text{A g}^{-1}$ . (D) Volumetric performance metrics of (BP-G)/PANI electrode compared with various state-of-the-art anodes. The volumetric capacities are calculated based on the gravimetric capacity and packing densities of the electrodes, including carbon black and binder. The data of the 10th cycle, which were considered the performance of an electrode after its initial aging process, were obtained from (A) and (C). The data of the 2000th cycle, which were considered the performance of an electrode at the end of its service life in practical LIBs, were obtained from (C). (E) Cycling performance of (BP-G)/PANI composite compared with different control samples.

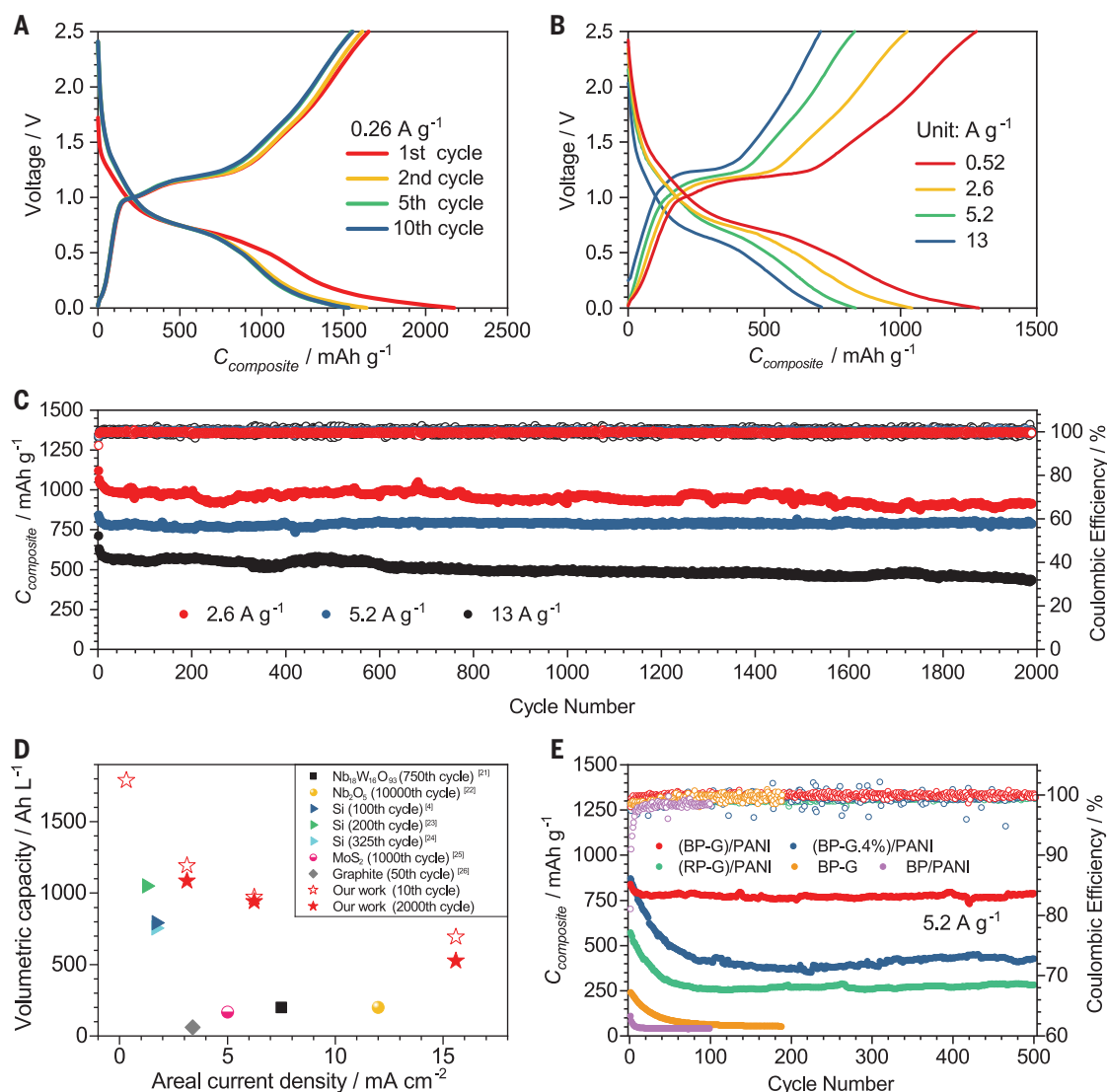
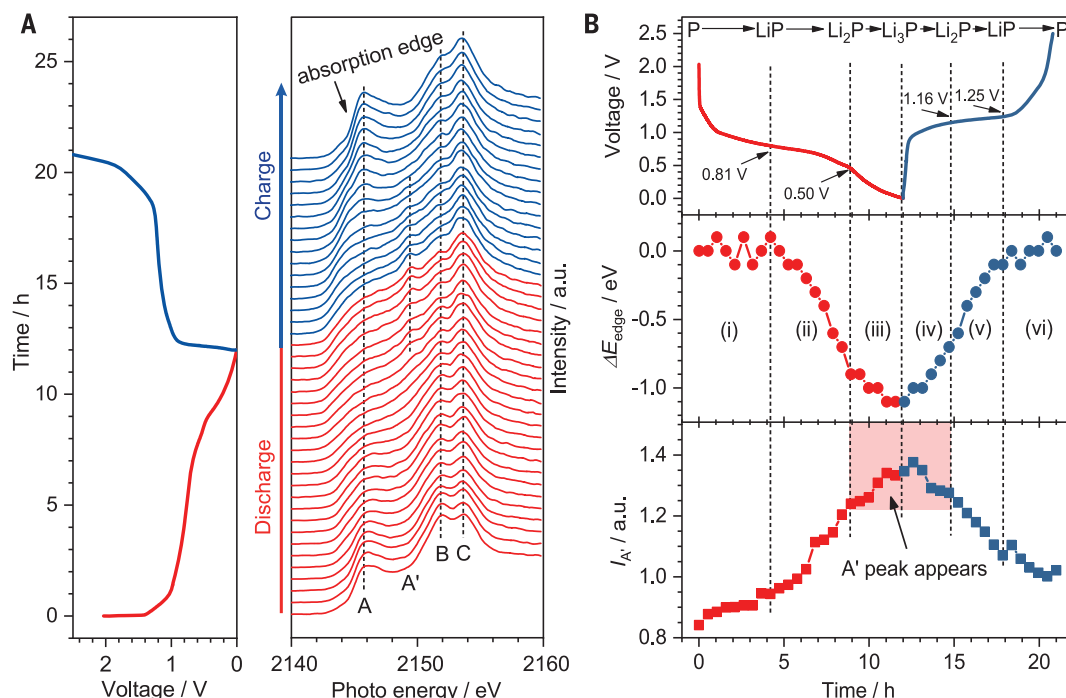


**Fig. 3. In situ XAS tracking of the structural evolution of BP-G electrodes.** (A) A series of XAS near-edge spectra for the P K-edge as a function of discharge-charge cycle time ( $t$ ), recorded from a BP-G electrode during the first galvanostatic lithiation-delithiation cycle at  $0.13 \text{ A g}^{-1}$ . The state of charge corresponds to the time scale of the voltage profile (left). (B) Relative shift of the absorption edge ( $\Delta E_{\text{edge}}$ ) and absorption intensity at peak A' as a function of discharge-charge time. The dashed lines divide six regions (indicated by lowercase roman numerals) based on the slope of the  $\Delta E_{\text{edge}} - t$  curve. The red area marks the region where peak A' appears.



that the basal planes of BP and graphite are intimately merged together.

The dark-field TEM image (Fig. 1F) shows the (BP-G)/PANI is composed of primarily particles with sizes of ~500 nm, and the elemental maps show a rather consistent distribution of P, C, and N with a morphology almost identical to that in the dark-field TEM image, indicating a uniform PANI coating.

### Li storage performance of (BP-G)/PANI

The synthesized (BP-G)/PANI (containing 65 wt % BP, 16 wt % graphite, and 19 wt % PANI) (materials and methods) was characterized by the constant current method in a voltage range of 0.001 to 2.5 V versus (Li/Li<sup>+</sup>). The gravimetric capacities and current densities were quantified by normalizing to the total mass of the entire composite. The (BP-G)/PANI delivered initial discharge and charge capacities of 2170 and 1650 mA·hour g<sup>-1</sup> at 0.26 A g<sup>-1</sup> (Fig. 2A), with an initial Coulombic efficiency of 76.0%. At the 10th cycle, the (BP-G)/PANI showed a reversible discharge capacity of 1520 mA·hour g<sup>-1</sup>. The discharge profiles measured during different cycles show a plateau at ~0.75 V (Fig. 2A), which is characteristic of the formation of Li<sub>x</sub>P (20). This plateau remains resolvable at increased discharge current densities of 0.52, 2.6, 5.2, and 13 A g<sup>-1</sup> (Fig. 2B), indicating excellent reaction kinetics between BP and Li<sup>+</sup>. To probe the dominant charge storage kinetics in (BP-G)/PANI, we analyzed the capacity contribution from the diffusion-controlled process and the capacitive process (fig. S3 and supplemen-

tary text S1). The pseudocapacitive process contributes a substantial (nearly constant) fraction of the overall capacity at low or high rates, which is beneficial to high-power operation.

We tested the cycling performance at different charge-discharge current densities (Fig. 2C). The (BP-G)/PANI anode (at an areal loading of 1.2 mg cm<sup>-2</sup>) showed a reversible capacity of 910 mA·hour g<sup>-1</sup> after cycling at 2.6 A g<sup>-1</sup> for 2000 cycles, a reversible capacity of 790 mA·hour g<sup>-1</sup> after cycling at 5.2 A g<sup>-1</sup> for 2000 cycles, and a reversible capacity of 440 mA·hour g<sup>-1</sup> after cycling at 13 A g<sup>-1</sup> for 2000 cycles. The ability to charge an anode material at 13 A g<sup>-1</sup> with a reversible capacity of 440 mA·hour g<sup>-1</sup> promises advanced LIBs that require <10-min charging to a cell-level energy density of ~350 W·hour kg<sup>-1</sup> (5). When the areal loadings were increased to 2.2 and 3.6 mg cm<sup>-2</sup>, the (BP-G)/PANI retained gravimetric capacities of 980 and 750 mA·hour g<sup>-1</sup>, respectively (fig. S4).

The electrochemical performance was obtained with a conventional slurry electrode structure consisting of (BP-G)/PANI, carbon black, and binder (materials and methods) at an overall packing density of  $1.49 \pm 0.08 \text{ g cm}^{-3}$ , which is close to that of a commercial graphite anode (table S2). The porosity of the (BP-G)/PANI anode is  $0.29 \pm 0.04$  (supplementary text S2). Once experimental gravimetric capacity and electrode packing density are considered, the (BP-G)/PANI presents a volumetric capacity of 1090 A·hour liter<sup>-1</sup> at 3.1 mA cm<sup>-2</sup> after 2000 cycles and 530 A·hour liter<sup>-1</sup> at

15.6 mA cm<sup>-2</sup> after 2000 cycles (Fig. 2D). Such high-rate performance, especially after extended cycling, exceeds those of traditional carbon anodes or advanced silicon anodes and is comparable with those of known high-rate materials (Fig. 2D and table S3) (4, 21–26), yet with a considerably higher capacity.

Taking the volumetric capacities of the whole anode (21), we can project the energy density with respect to the volume of the (BP-G)/PANI anode, to reach up to 1940 W·hour liter<sup>-1</sup> at a power density of 50 kW liter<sup>-1</sup> (fig. S5 and supplementary text S3). A prototype full cell comprised of a LiCoO<sub>2</sub> cathode and a (BP-G)/PANI anode shows comparable performance to that in half-cells (fig. S6).

To elucidate the roles of BP, graphite, and PANI in the (BP-G)/PANI for Li storage, we prepared four different composites (materials and methods): (i) red phosphorus (RP)-based ternary composites, (RP-G)/PANI; (ii) (BP-G.4%)/PANI (containing less graphite content, 4 wt %); (iii) BP-G; and (iv) BP/PANI. Their structures and cyclic voltammetry (CV) profiles are shown in figs. S7 and S8, and their cycling performances are compared in Fig. 2E. The discharge capacity of (BP-G)/PANI is around three times that of (RP-G)/PANI at the same rate, suggesting that BP contributes to at least 70% of the capacity of (BP-G)/PANI. The reversible capacities of the composites decreased with decreasing graphite content in the order (BP-G)/PANI > (BP-G.4%)/PANI > BP/PANI (Fig. 2E), even though (BP-G)/PANI contained the lowest mass of BP (65 wt %) and thus the lowest theoretical capacity, which



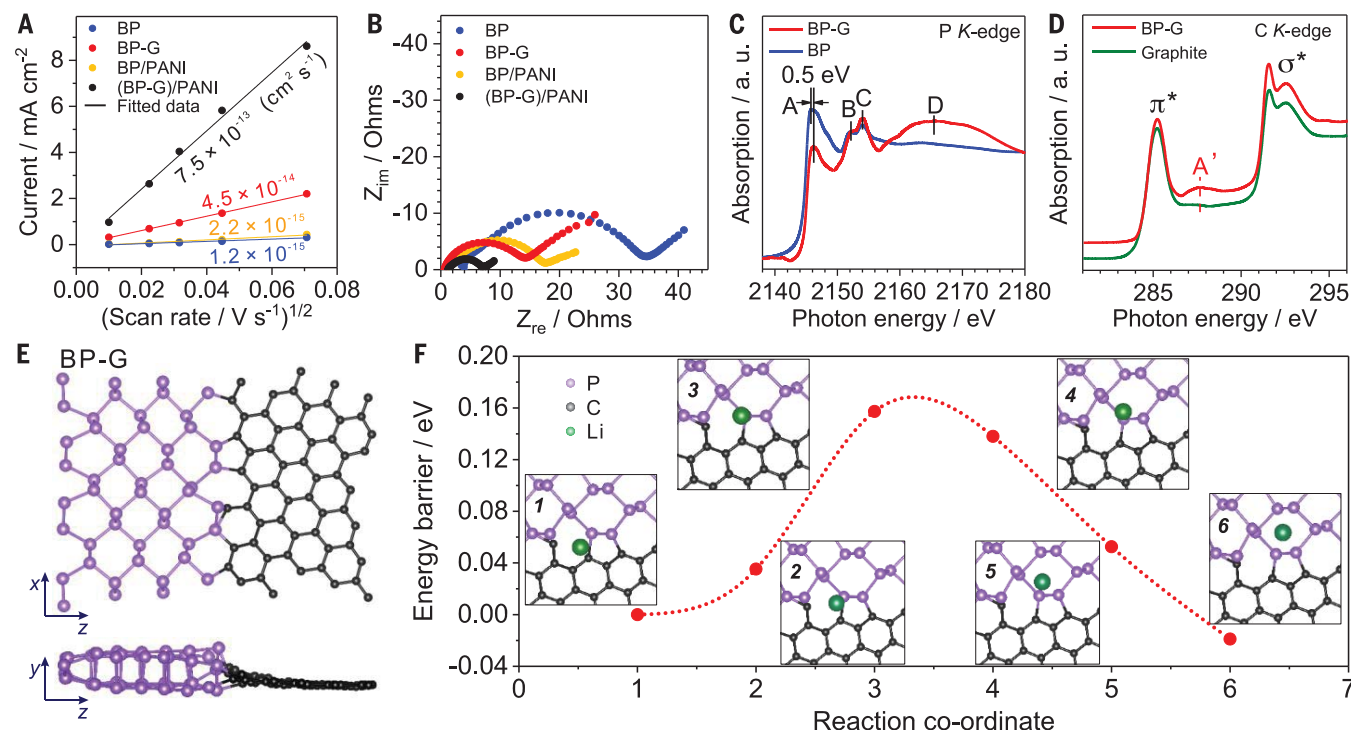


**Fig. 4. Charge transfer properties and structure of BP-G.** (A and B)  $D_{Li}$  values derived from the CV profiles (A) and Nyquist plots (B) of (BP-G)/PANI, BP-G, BP/PANI, and BP. (C and D) P K-edge XAS spectra of BP-G and BP (C) and C K-edge XAS spectra of BP-G and graphite (D). (E) Schematic of BP-G hybrid structure with in plane P-C bonds. (F) The minimum energy pathways for  $Li^+$  to diffuse through the BP-G boundary. The results shown in (E) and (F) were obtained from the DFT calculations.

demonstrates the important role of graphite in facilitating Li storage in BP. Moreover, the reversible capacity of (BP-G)/PANI is ~10 times that of BP-G, demonstrating the role of PANI in preserving the cycling stability of BP.

### The role of BP-G bonding

To further probe the role of graphite in Li storage, we performed in situ x-ray absorption spectroscopy (XAS) measurements on BP-G electrodes (Fig. 3). The voltage profile shows discharge and charge plateaus at ~0.75 and ~1.20 V, respectively (Fig. 3A), which is much higher than the (de)lithiation voltage of graphite [~0.1 V versus (Li/Li<sup>+</sup>)]. Therefore, Li reacts predominantly with BP during in situ XAS measurements. At the beginning of discharge, the absorption edge is located at 2144.3 eV, with three edge peaks, A, B, and C, evident in the P K-edge XAS spectrum at 2146.2, 2152.0, and 2153.7 eV, respectively (Fig. 3A). In the whole discharge-charge process, the positions of peaks B and C do not change, whereas the absorption edge shifts [defined by  $\Delta E_{edge} = E(t) - E(0)$ , where  $E(t)$  and  $E(0)$  are the positions of absorption edges in the spectra of intermediate and initial states, respectively], and a new peak, A', appears at the discharge-charge time ( $t$ ) of 8.9 to 14.8 hours.

The  $\Delta E_{edge} - t$  curve is plotted together with the voltage profile of the BP-G electrode in Fig. 3B. According to the slope of the curve,

there are three regions in the discharge process: (region i)  $t < 4.2$  hours, where  $\Delta E_{edge}$  is ~0.0 eV; (region ii)  $4.2 < t < 8.9$  hours, where  $\Delta E_{edge}$  evolves rapidly to ~0.9 eV; and (region iii)  $8.9 < t < 11.9$  hours, where  $\Delta E_{edge}$  evolves slowly to ~1.1 eV at the end of discharge ( $t = 11.9$  hours). The voltages at  $t$  of 4.2, 8.9, and 11.9 hours are 0.81, 0.50, and 0.01 V, respectively, matching those of LiP, Li<sub>2</sub>P, and Li<sub>3</sub>P in the discharge profile (20) and the XRD measurements (fig. S9). The red shift of the absorption edge of the P K-edge spectrum indicates electron acceptance of P atoms (27). The little change in  $\Delta E_{edge}$  in region i indicates that the phase change between P and LiP involves only a weak bonding between Li and P atoms (28) and high reversibility of the phase change between P and LiP (7). The formation of Li<sub>2</sub>P is accompanied by a large evolution of  $\Delta E_{edge}$  (Fig. 3B, region ii) because of the substantial structural distortion of BP and the increased number of Li-P bonds in Li<sub>2</sub>P (20). Li<sub>3</sub>P has a hexagonal layered structure (P6<sub>3</sub>/mmc) consisting of alternatively arranged Li and Li<sub>2</sub>P layers (29); the change of  $\Delta E_{edge}$  is only 0.2 eV from Li<sub>2</sub>P to Li<sub>3</sub>P, but the phase change from Li<sub>2</sub>P to Li<sub>3</sub>P leads to the appearance and growth of an A' peak at 2149.5 eV.

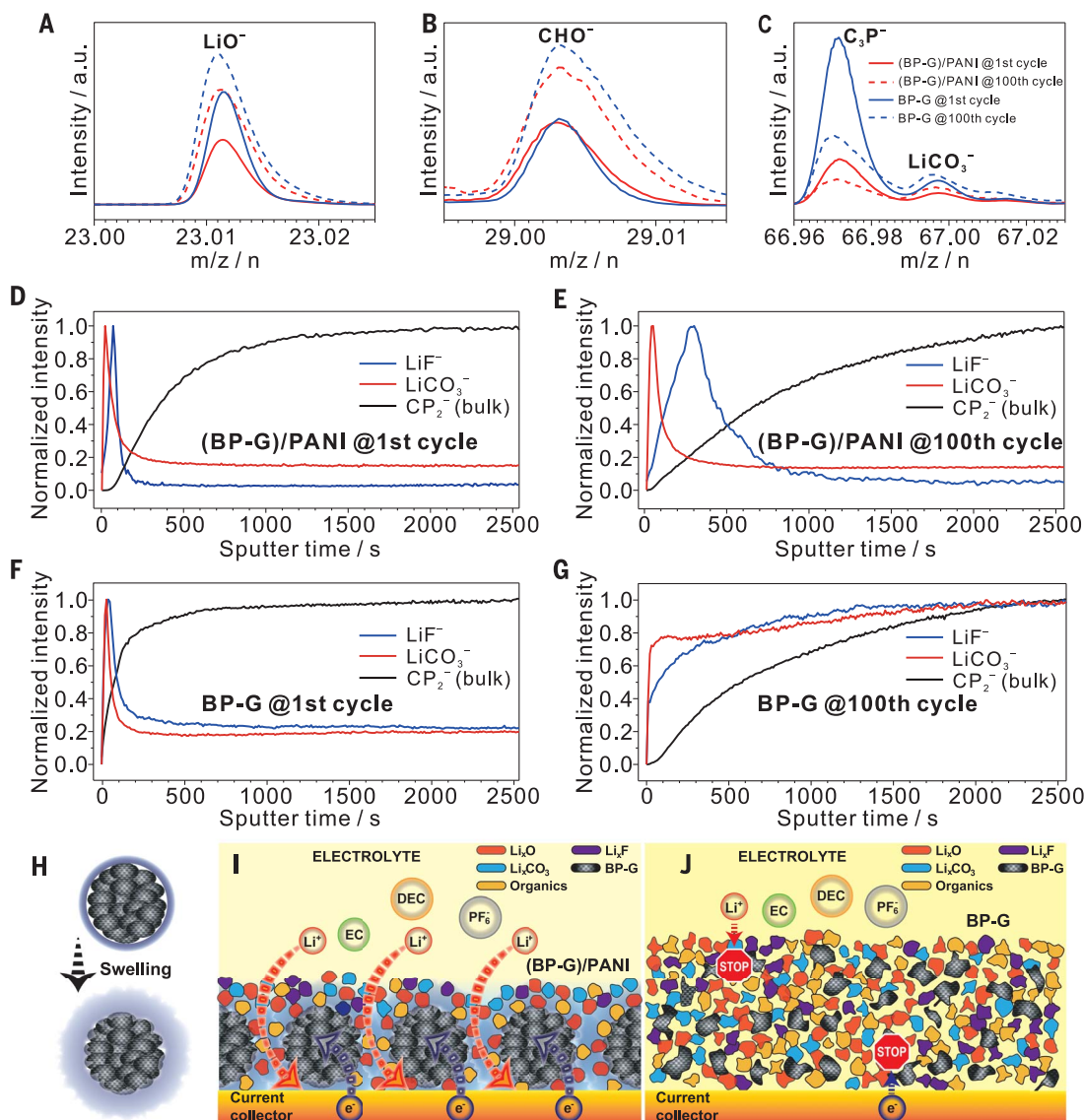
During charging, the  $\Delta E_{edge}$  shows an essentially symmetric profile with a slow increase to ~0.7 eV at 14.8 hours (Fig. 3B, region iv), then a more rapid increase to around 0.0 eV

at 17.9 hours (Fig. 3B, region v), and then stays at 0.0 eV from 17.9 to 21.0 hours (Fig. 3B, region vi). The intensity of peak A' shows a similar mirror evolution as a function of discharge and charge time. The reversible increase and decrease of  $\Delta E_{edge}$  and the intensity of peak A' with a symmetric profile during the charge and discharge process indicate that the phase change between BP and Li<sub>3</sub>P in BP-G is highly reversible. The change of the XAS spectra with the state of charge of the bare BP was much smaller (fig. S10), suggesting a considerably lower lithiation level of BP than BP-G. Together, these in situ studies demonstrate that the presence of graphite in the BP-G hybrid allows a deeper and more reversible (de)lithiation of BP, which contributes to the improved Li storage performance.

We conducted CV and electrical impedance spectroscopy (EIS) studies and compared the results with those for several control electrodes, including (BP-G)/PANI, BP-G, BP/PANI, and BP (fig. S8). The derived Li<sup>+</sup> diffusion coefficients ( $D_{Li}$ ) in BP-G ( $4.5 \times 10^{-14} \text{ cm}^2 \text{ s}^{-1}$ ) and (BP-G)/PANI ( $7.5 \times 10^{-13} \text{ cm}^2 \text{ s}^{-1}$ ) are one to two orders of magnitude higher than that in BP ( $1.2 \times 10^{-15} \text{ cm}^2 \text{ s}^{-1}$ ) and BP/PANI ( $2.2 \times 10^{-15} \text{ cm}^2 \text{ s}^{-1}$ ) (Fig. 4A and supplementary text S4). The charge transfer resistance ( $R_{ct}$ ) in BP-G (13.7 ohms) and (BP-G)/PANI (5.9 ohms) is considerably lower than that in BP (31.1 ohms) (Fig. 4B, fig. S8, and table S4). The higher  $D_{Li}$

**Fig. 5. Interfacial study of (BP-G)/PANI and BP-G anodes. (A to C)** ToF-SIMS spectra of secondary ion fragments  $\text{LiO}^-$  (A)  $\text{CHO}^-$  (B), and  $\text{C}_3\text{P}^-$  and  $\text{LiCO}_3^-$  (C) collected from the cycled (BP-G)/PANI and BP-G electrodes.

**(D to G)** Normalized depth profiles of some representative secondary ion fragments obtained from the (BP-G)/PANI anode after the first cycle (D) and after the 100th cycle (E), and from the BP-G anode after the first cycle (F) and after the 100th cycle (G). **(H)** Schematic of electrolyte-swollen BP-G coated with PANI. **(I and J)** Schematics of the (BP-G)/PANI electrode, in which the PANI coating helps retain a stable SEI (I) to prevent continuous formation of poorly conducting Li fluorides and carbonates deep into the BP-G particles (J).



and lower  $R_{\text{ct}}$  of BP-G hybrids are consistent with the in situ XAS results showing that graphite improves the completeness and reversibility of the lithiation reaction, which contributes to the improved rate capability and cycling stability. Beyond the electrochemical benefits, the efficient ion transport and reduced overall impedance of the composite together with the high thermal conductivity of the BP and G may also help minimize heat generation and accelerate heat dissipation during high-rate operation (supplementary text S5), which is beneficial for cycling stability and battery safety.

Previous theoretical calculations have indicated that the wide channel and low diffusion barrier along the zigzag direction of BP are responsible for the high  $D_{\text{Li}}$  in BP (12). However, theoretical calculations (30) also suggest that reconstruction at the BP edges (the

curving of the basal planes, as also confirmed by TEM observation) (14) results in a narrower gap for  $\text{Li}^+$  diffusion and thus limits its performance. We believe that the formation of P-C bonds between BP and graphite flakes (during the ball milling process) mitigates the edge reconstruction problem, and this is supported by the TEM images (Fig. 1, D and E) and XAS analysis (Fig. 4, C and D) and also the density functional theory (DFT) calculation (Fig. 4, E and F). The P  $K$ -edge XAS spectra show four distinguishable peaks: A, B, C, and D (Fig. 4C). The peak A of BP-G (2146.2 eV) has a photon energy higher than that of BP (2145.7 eV) (31), which is in agreement with the P  $L$ -edge spectra (fig. S11A and supplementary text S6) and is more likely attributable to charge transfer from a P atom to a C or H atom rather than P-O bonding (with a typical photon energy of >2147.0 eV) (32). Addi-

tionally, elemental analysis (table S1) shows that both BP and BP-G have negligible amounts of hydrogen. Hence, peak A is exclusively ascribed to P-C bonding. A broad peak (D) at  $\sim 2165.0$  eV appears in the XAS of BP-G (Fig. 4C) but not in that of BP; this has been attributed to the distortion of the P site by the neighboring C atoms in P-doped diamond (33). Similarly, the peak A' in the C  $K$ -edge XAS (Fig. 4D) is assigned exclusively to C-P bonding due to the exclusion of C-O bonding (fig. S11B, XPS spectrum) and C-H bonding (table S1). The apparent excitonic state and  $\sigma^*$  state in the C  $K$ -edge XAS (Fig. 4D and supplementary text S6) indicate that the graphite lattice remains a well-ordered planar structure after the synthesis of BP-G. If a P atom is connected to graphite perpendicularly by  $\pi$  bonding, the  $\pi^*$  absorption feature (285.4 eV) (Fig. 4D) should become broad, or even split. These analyses suggest the

BP and graphite are mostly connected by BP-G  $\sigma$  bonds at the edge of the basal plane, which is consistent with the high-resolution TEM studies (Fig. 1E).

Our DFT calculation (materials and methods) suggests that the BP-G bonding is an exothermic process with a formation energy of  $-2.01$  eV per P-C bond (Fig. 4E). Notably, our calculation also shows that the energy barrier for  $\text{Li}^+$  migration into BP through a graphite-BP boundary is  $0.16$  eV (Fig. 4F), which is considerably lower than that for  $\text{Li}^+$  migration across a reconstructed BP edge ( $0.52$  eV) (fig. S12). The BP-G bonding is thus essential for retaining open channels for  $\text{Li}^+$  entry into the BP flakes, leading to an improved  $D_{\text{Li}}$  for high-rate operation. By physically mixing BP with graphite or Ketjen Black (KB) and a subsequent PANI coating, we prepared two more control materials, (BP/G)/PANI and (BP/KB)/PANI, which showed inferior Li storage performance (fig. S13 and supplementary text S7) to that of the covalently bonded (BP-G)/PANI. The  $D_{\text{Li}}$  of the control samples is also about two orders of magnitude lower than that of (BP-G)/PANI. The physical mixing of graphitized carbon and BP does not create sufficient quantities of P-C bonds to restrain BP edge reconstruction, and this leads to sluggish charge transfer across the BP edges.

### The role of PANI

To reveal the function of PANI, we conducted time-of-flight-secondary ion mass spectrometry (ToF-SIMS) studies on pristine and cycled (BP-G)/PANI and BP-G electrodes to visualize the chemical evolution occurring at the electrode-electrolyte interface (materials and methods and fig. S14). The N-containing secondary ion fragments ( $^{13}\text{CN}^-$  and  $\text{C}_2\text{N}^-$ ) are attributed to PANI, the P-containing species ( $\text{CP}_2^-$ ,  $\text{C}_5\text{P}^-$ , and  $\text{P}_2^-$ ) to BP, and the  $\text{C}_6^-$  to graphite (fig. S15). The uncycled (BP-G)/PANI electrode shows a considerably stronger signal for N-containing species (fig. S15, A and B) and a much weaker signal for P-containing species (fig. S15, C to E) and  $\text{C}_6^-$  (fig. S15F) than BP-G, demonstrating the PANI coating on (BP-G)/PANI. Upon cycling, the signals that stand for the key components of SEI ( $\text{LiO}^-$ ,  $\text{CHO}^-$ , and  $\text{LiCO}_3^-$ ) are intensified (Fig. 5, A to C), whereas the signals for P-containing species (Fig. 5C and fig. S16, A and B), which stand for electrode materials, are attenuated. The SEI signals of (BP-G)/PANI are apparently lower than those of BP-G after the same number of cycles (Fig. 5, A to C), indicating inhibited SEI growth on (BP-G)/PANI.

To probe the SEI evolution upon cycling, we collected ToF-SIMS depth profiles from the cycled BP-G and (BP-G)/PANI electrodes (Fig. 5, D to G, and fig. S17). After the first cycle, sharp peak signals of  $\text{LiO}^-$ ,  $\text{LiCO}_3^-$ , and  $\text{LiF}^-$  (which separately denote Li oxides, carbonates,

and fluorides) were detected at the lowest sputter depth (Fig. 5, D and F, and fig. S17, A and C) for both electrodes, suggesting SEI formation. After 100 cycles, the  $\text{LiO}^-$ ,  $\text{LiF}^-$ , and  $\text{LiCO}_3^-$  signals remained at a peak at the electrode surface of (BP-G)/PANI, yet they were found all the way into the bulk of the BP-G electrode (Fig. 5, E and G, and fig. S17, B and D), suggesting deep penetration of poorly conducting SEI species (e.g., Li fluorides and carbonates).

These studies show that the PANI coating ensures a stable SEI and prevents continued buildup of poorly conducting species, which may be largely attributable to protection and mediation by a thin layer of PANI swollen with electrolyte (Fig. 5H). The swollen PANI is directly evidenced by the increase in thickness of a PANI disc after immersion into the electrolyte (fig. S18) and is supported by the ToF-SIMS depth profiles of the (BP-G)/PANI electrode at different cycling stages (fig. S16, C and D, fig. S19, and supplementary text S8). The swollen PANI also enables doping of the polymer matrix with  $\text{Li}^+$  and protons and uptake of corrosive hydrogen fluoride (fig. S16, E and F, and supplementary text S9) to facilitate charge transport throughout the electrode (Fig. 5I, fig. S20, and supplementary text S10) (16, 34). The inhibited formation of Li fluorides and carbonates and the increased conductivity of swollen PANI facilitate charge transfer at the electrode-electrolyte interface (35). Without the PANI coating, the Li fluorides and carbonates build up appreciably (Fig. 5, G and J), degrading the charge transport. Benefiting from the optimized interface design, the (BP-G)/PANI composites retain a stable structure upon cycling, with little change in morphology, electrode thickness, and elemental distributions in the cycled electrode (fig. S21 and supplementary text S11).

By carefully engineering the BP-G interface and (BP-G)/PANI-electrolyte interface, we show that the charge (electron and ion) transport in the composite electrode can be optimized to ensure efficient utilization of the lithium storage capacity of BP under an ultrahigh rate, delivering a combination of high rate, high capacity, and robust cycling performance.

### REFERENCES AND NOTES

1. J. B. Goodenough, K.-S. Park, *J. Am. Chem. Soc.* **135**, 1167–1176 (2013).
2. Y. Gogotsi, P. Simon, *Science* **334**, 917–918 (2011).
3. Y. Liu, G. Zhou, K. Liu, Y. Cui, *Acc. Chem. Res.* **50**, 2895–2905 (2017).
4. M. Ko et al., *Nat. Energy* **1**, 16113 (2016).
5. E. J. Berg, C. Villavieille, D. Streich, S. Trabesinger, P. Novák, *J. Electrochem. Soc.* **162**, A2468–A2475 (2015).
6. C. Zhu, R. E. Usiskin, Y. Yu, J. Maier, *Science* **358**, eaao2808 (2017).
7. C.-M. Park, H.-J. Sohn, *Adv. Mater.* **19**, 2465–2468 (2007).
8. X. Ling, H. Wang, S. Huang, F. Xia, M. S. Dresselhaus, *Proc. Natl. Acad. Sci. U.S.A.* **112**, 4523–4530 (2015).
9. M. S. Whittingham, *Proc. IEEE* **100**, 1518–1534 (2012).
10. J. Sun et al., *Nano Lett.* **14**, 4573–4580 (2014).

11. J. H. Ryu, J. W. Kim, Y.-E. Sung, S. M. Oh, *Electrochem. Solid-State Lett.* **7**, A306–A309 (2004).
12. W. Li, Y. Yang, G. Zhang, Y.-W. Zhang, *Nano Lett.* **15**, 1691–1697 (2015).
13. Q. Zhang, W. Zhang, W. Wan, Y. Cui, E. Wang, *Nano Lett.* **10**, 3243–3249 (2010).
14. Y. Lee et al., *J. Phys. D Appl. Phys.* **50**, 084003 (2017).
15. J. Wu, N. Mao, L. Xie, H. Xu, J. Zhang, *Angew. Chem. Int. Ed.* **54**, 2366–2369 (2015).
16. G. Ćirić-Marjanović, *Synth. Met.* **177**, 1–47 (2013).
17. M. S. Dresselhaus, A. Jorio, R. Saito, *Annu. Rev. Condens. Matter Phys.* **1**, 89–108 (2010).
18. H. S. Lipson, A. R. Stokes, *Proc. R. Soc. A* **181**, 101–105 (1942).
19. Z. Zhang et al., *Science* **357**, 788–792 (2017).
20. M. Mayo, K. J. Griffith, C. J. Pickard, A. J. Morris, *Chem. Mater.* **28**, 2011–2021 (2016).
21. K. J. Griffith, K. M. Wiaderek, G. Cibin, L. E. Marbella, C. P. Grey, *Nature* **559**, 556–563 (2018).
22. H. Sun et al., *Science* **356**, 599–604 (2017).
23. S. Choi, T.-W. Kwon, A. Coskun, J. W. Choi, *Science* **357**, 279–283 (2017).
24. Y. Li et al., *Nat. Energy* **1**, 15029 (2016).
25. Y. M. Chen, X. Y. Yu, Z. Li, U. Paik, X. W. Lou, *Sci. Adv.* **2**, e1600021 (2016).
26. J. Billaud, F. Bouville, T. Magrini, C. Villavieille, A. R. Studart, *Nat. Energy* **1**, 16097 (2016).
27. P. E. Blanchard, A. P. Grosvenor, R. G. Cavell, A. Mar, *J. Mater. Chem.* **19**, 6015–6022 (2009).
28. W. Hönle, H. G. von Schnering, *Z. Kristallogr. Cryst. Mater.* **155**, 307–314 (1981).
29. Y. Dong, F. J. DiSalvo, *Acta Crystallogr. Sect. E Struct. Rep. Online* **63**, i97–i98 (2007).
30. H. B. Ribeiro et al., *Nat. Commun.* **7**, 12191 (2016).
31. K. Nakanishi, T. Ohta, *J. Phys. Condens. Matter* **21**, 104214 (2009).
32. R. G. Cavell, A. Jürgensen, *J. Electron Spectrosc. Relat. Phenom.* **101–103**, 125–129 (1999).
33. S. Shikata et al., *Appl. Phys. Lett.* **110**, 072106 (2017).
34. M. Wan, J. Yang, *J. Appl. Polym. Sci.* **55**, 399–405 (1995).
35. T. Liu et al., *Nat. Nanotechnol.* **14**, 50–56 (2019).

### ACKNOWLEDGMENTS

The authors thank L.-J. Wan from the Institute of Chemistry, CAS, and Y. Luo from USTC for insightful discussion regarding the electrochemistry and phase evolution of BP, and also K.-C. Jiang from Jiangsu TAFEL New Energy Technology for sharing his industry viewpoint about BP. **Funding:** He.J. appreciates funding support from the Natural Science Foundation of China (51672262, 21975243, and 51761145046). S.X. acknowledges financial support from the National Key R&D Program of China (2019YFA0705600). C.C. acknowledges financial support from MOST project 104-2112-M-032-005-MY2. X.W. acknowledges financial support from MOST (2016YFA0200602 and 2018YFA0208603), NSFC (21573204), and Anhui Initiative in Quantum Information Technologies. J.B.G. acknowledges the Lawrence Berkeley National Laboratory BMR Program (grant 7223523). **Author contributions:** He.J. and X.D. designed the research. He.J. and Ho.J. conceived the experiments. Ho.J. conducted the materials preparation. Ho.J., S.X., J.Z., and Z.Q. conducted the electrochemical measurements and/or contributed to data analysis. Ho.J., C.C., W.Y., Y.-R.L., and T.-S.C. conducted the XAS experiments and data analysis. S.X. and W.L. conducted ToF-SIMS experiments and data analysis. X.W., H.W., and Y.W. performed the DFT calculations. H.X. and T.Z. provided black phosphorus materials. He.J., X.D., S.X., Ho.J., and J.B.G. wrote the paper, and all authors were involved in revising the manuscript. **Competing interests:** The authors declare that they have no competing interests. **Data and materials availability:** All data are available in the manuscript or the supplementary materials.

### SUPPLEMENTARY MATERIALS

science.sciencemag.org/content/370/6513/192/suppl/DC1  
Materials and Methods  
Supplementary Text S1 to S11  
Figs. S1 to S21  
Tables S1 to S4  
References (36–50)

30 September 2018; resubmitted 27 March 2019  
Accepted 6 August 2020  
10.1126/science.aav5842



## Black phosphorus composites with engineered interfaces for high-rate high-capacity lithium storage

Hongchang JinSen XinChenghao ChuangWangda LiHaiyun WangJian ZhuHuanyu XieTaiming ZhangYangyang  
WanZhikai QiWensheng YanYing-Rui LuTing-Shan ChanXiaoJun WuJohn B. GoodenoughHengxing JiXiangfeng Duan

*Science*, 370 (6513), • DOI: 10.1126/science.aav5842

### Engineering phosphorous anodes

A focus of battery research has been the development of a range of lithium, sodium, and potassium cathodes, but improving anode materials is also an important goal. Silicon has shown some promise for replacing graphite because of its exceptional capacity, but the dramatic volume change during lithiation-delithiation processes often leads to failure. Jin *et al.* developed a composite that is made of black phosphorous and graphite in its core and covered with swollen polyaniline. In contrast to previous efforts, bonding between the carbon and phosphorous allows for a high charging rate without sacrifices in capacity and cycling stability.

*Science*, this issue p. 192

### View the article online

<https://www.science.org/doi/10.1126/science.aav5842>

### Permissions

<https://www.science.org/help/reprints-and-permissions>

Use of this article is subject to the [Terms of service](#)